Fuel Processing Technology 278 (2025) 108340

Contents lists available at ScienceDirect

Fuel Processing Technology

journal homepage: www.elsevier.com/locate/fuproc

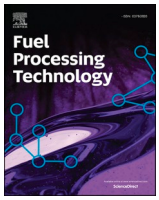

Machine learning-driven modeling framework for steam co-gasification applications

Usman Khan Jadoon, Ismael Díaz, Manuel Rodríguez *

Departamento de Ingeniería Química Industrial y del Medioambiente, Escuela Técnica Superior de Ingenieros Industriales, Universidad Politécnica de Madrid, C/ José Gutiérrez Abascal 2, 28006 Madrid, Spain

ARTICLE INFO

Keywords:
Co-gasification
First-principle modeling
Machine learning
Syngas prediction
Sensitivity analysis
Explainable AI

ABSTRACT

Steam co-gasification of biomass and plastic waste is a promising route for syngas production and waste valorization. However, accurately predicting syngas composition remains challenging due to inherent complexity and nonlinearity of the process. This study presents a comprehensive comparative analysis between conventional process simulators-based models (Aspen Plus), namely the thermodynamic equilibrium (TEM), restricted thermodynamic (RTM), and kinetic (KM) modeling approaches, and machine learning (ML) models for the prediction of the syngas composition. Using 208 experimental data points compiled from 20 published studies covering various feedstocks and gasification conditions in bubbling fluidized bed gasifiers (BFBG), the performance of the models was evaluated after extensive data preprocessing. Among several ML algorithms evaluated, the neural network (NN) delivered the lowest average root mean square error in syngas mol fraction predictions (0.0174), outperforming RTM (0.0966), KM (0.1378), and TEM (0.1470). To explore input–output relationships beyond interpolation, a conditional generative adversarial network (cGAN) generated synthetic data, which served as the basis for sensitivity and interpretability analyses. The NN, acting as a surrogate model, was paired with SHapley Additive exPlanations (SHAP) and Partial Dependence Plots (PDP) to quantify the effects and nonlinear interactions of key features on syngas yields providing actionable insights for process optimization.

1. Introduction

The urgent global energy transition toward sustainable, low-carbon systems to meet international climate targets for 2030 and 2050 has intensified interest in alternatives to fossil fuels, whose continued use accelerates resource depletion and greenhouse gas emissions [1,2]. Among emerging strategies, the thermochemical conversion of waste materials, including biomass and plastic residues, offers the dual benefit of clean energy production and environmental remediation. Notably, co-gasification using steam as the fluidizing medium has gained traction as a versatile route to generate high-quality synthesis gas (syngas), suitable for downstream applications such as electricity generation, synthetic fuel production, or chemical manufacturing [3].

Biomass, owing to its renewability and carbon neutrality, is a promising feedstock. However, its standalone application is often limited by inherent drawbacks such as high moisture and oxygen content, low energy density, and inconsistent supply [4]. To overcome these limitations, co-gasifying biomass with high-energy-density municipal solid waste (MSW), especially plastic waste, has been shown to enhance gasification efficiency, improve syngas composition, and contribute to effective waste valorization [3]. This integrated approach addresses both energy security and the increasing global challenge of plastic waste, positioning co-gasification as a viable solution within circular economy and decarbonization frameworks.

Thermochemical conversion processes are recognized for their ability to efficiently convert carbonaceous feedstocks into energy-rich syngas. BFBG have emerged as a superior technology for the steam-O_2 gasification of biomass and plastic waste, offering significant advantages over alternative reactor designs. These systems excel in providing uniform temperature distribution, efficient heat and mass transfer, and excellent mixing characteristics, which are crucial for efficient gasification [5]. The ability to maintain near-constant temperatures and operate with high flexibility makes fluidized beds particularly well-suited for handling heterogeneous feedstocks such as biomass and waste materials [5]. Furthermore, these reactors demonstrate remarkable versatility in terms of feedstock calorific value, moisture content, particle size, and density, allowing the processing of a wide range of materials, including low-rank coals, lignite, and several types of solid

* Corresponding author.
E-mail address: manuel.rodriguezh@upm.es (M. Rodríguez).

https://doi.org/10.1016/j.fuproc.2025.108340
Received 21 July 2025; Received in revised form 9 September 2025; Accepted 15 September 2025
Available online 19 September 2025

recovered fuels [6,7]. The enhanced gas-solid contact in fluidized beds promotes higher conversion rates and yields of desired products, such as syngas, while minimizing the formation of unwanted byproducts [8]. Additionally, the ability to operate in continuous mode with the potential for scaling up to high throughput makes fluidized bed reactors an attractive option for industrial-scale gasification processes [5]. Despite some challenges, such as the need for larger reactor sizes and potential particle entrainment, the general advantages of BFBG in terms of process efficiency, product quality, and operational flexibility position them as a pivotal technology for advancing the field of biomass and plastic waste gasification [9].

When gasifying agents are introduced such as air, steam, O_2, CO_2, or any mixture of these, the process enables the decomposition of complex materials into simpler and combustible gases. Air gasification has been extensively studied; however, it produces a gas with a low heating value (LHV) of only 4–6 MJ/m^3 and an H_2 content of 8–14 vol% [10]. Oxygen-enriched air gasification can generate medium heating value (MHV) gas but requires costly O_2 production infrastructure, limiting large-scale adoption. In contrast, extensive experimental studies have shown that steam gasification can yield an MHV of up to 16 MJ/Nm^3 and H_2 concentrations of up to 60 % [4,11,12]. This technology requires that the temperature of steam be over 700 °C, which demands additional cost for steam generator [13]. However, the steam-only gasification has some disadvantages as well as steam has low reactivity compared to O_2 [14]. Meanwhile, CO_2 gasification is drawing attention recently for its carbon conversion and cold gas efficiency over the aforementioned agents [15,16]. CO_2 gasification is not investigated much yet, but a mixture of O_2-CO_2 and steam-CO_2 has been conducted in various reactors. Flori et al. (2024) investigated the experimental assessment of varying O_2-CO_2 in downdraft gasifier and found out that it can produce N_2 free syngas flow rate ranging from 15 to 25 Nm^3/h, with a LHV between 8 and 10 MJ/Nm^3, and a cold gas efficiency of up to 78 % [17].

1.1. Modeling approaches for gasification

A crucial step toward advancing thermochemical processes is the development of robust models to support design, optimization, and scale-up. Gasification models serve to estimate product yields, evaluate performance, and guide operational control [18]. However, accurately simulating these systems is difficult owing to the intricate reaction networks and diversity of output streams. Consequently, multiple modeling methodologies have been developed to predict thermochemical behavior and syngas composition.

Equilibrium models based on Gibbs free energy minimization have been widely applied in process simulators such as Aspen Plus. For example, Ajorloo et al. (2025) simulated the co-gasification of biomass and plastic waste in BFBG using equilibrium and modified equilibrium models, with experimental validation [19]. Shi et al. (2025) used a kinetic modeling approach by steam and air simulation of biomass in BFBG using Aspen Plus environment [20]. Jadoon et al. (2025) conducted a comprehensive comparative analysis of woody biomass gasification in air using thermodynamic equilibrium, stoichiometric, and kinetic models implemented in commercial process simulators [21]. On the other hand Bhattarai et al. (2025) studied the co-gasification of biomass and plastic by kinetic models which were implemented in a 2D Eulerian computational fluid dynamics (CFD) model [22]. Similarly, Gupta et al. (2021) conducted the CFD studies of rice husk gasification in BFBG by using open FOAM [23]. In addition Wodołażski et al. (2020) conducted kinetic based biomass gasification by using CHEMCAD [24]. Furthermore, Escalante et al. (2025) studied the biomass and high-density polyethylene co-gasification via statistical methods (Taguchi), and ML [25].

These modeling platforms enable detailed analysis of chemical kinetics, multiphase flows, and transport phenomena, thereby supporting accurate prediction of syngas composition, identification of optimal operating parameters, and improvements in process economics. Moreover, both process simulator and data-driven ML approaches provide considerable benefits for syngas prediction in biomass thermochemical conversion. On one hand, ML methods offer high flexibility to fit available experimental data, low execution times, and are often implemented in open-source solutions. On the other hand, thermodynamic and kinetic modeling relies on well-established mathematical formulations designed to capture the physical and chemical phenomena involved in gasification processes, making them highly interpretable and generally applicable, although often computationally intensive and dependent on commercially licensed software [26].

Thermodynamic models are simple to implement (zero dimension), as they are based on temperature and pressure but independent of the reactor configuration. Niu et al. (2013), Zhu et al. (2016), Shahbaz et al. (2017), and Abdelrahim et al. (2019) investigated the gasification of MSW, palm kernel shells, and biosolids for syngas production, respectively, using thermodynamic modeling in BFBGs [27–30]. However, due to inherent limitations in their underlying assumptions, these models tend to mis predict the syngas outputs. Moreover, they fail to provide an accurate representation of the gasification process under conditions where kinetic and hydrodynamic effects play a dominant role [31]. Kinetic models excel at capturing non-equilibrium dynamics and typically produce more precise syngas composition estimates than equilibrium-based methods. Singh et al. (2022), Cao et al. (2024), and Wu et al. (2024) investigated the co-gasification of biomass and waste co-gasification in Aspen Plus by kinetic modeling [32–34]. On the other hand Nikoo et al. (2008), Beheshti et al. (2015), and Nguyen et al. (2021) investigated the biomass and plastic co-gasification kinetic based and in conjunction with the hydrodynamics of the system [35–37]. However, such models are system-specific and necessitate thorough datasets to calibrate and validate their kinetic parameters.

1.2. Emergence of ML and explainable AI

Given the limitations of traditional modeling, ML has emerged as a powerful and flexible alternative for gasification modeling. ML can capture complex non-linear relationships across diverse feedstocks and operating conditions, achieving high predictive accuracy with relatively low computational costs. For example, Cakar et al. (2025) trained various ML models on varying dataset sizes, with Random Forest (RF) demonstrating high accuracy with limited data ($R^2 = 0.985$ for H_2, 0.99 for exergy) [38]. However, under 10-fold cross-validation, RF showed strong robustness ($R^2 = 0.93$ for exergy), while Gaussian process regression achieved the highest H_2 prediction accuracy ($R^2 = 0.999$). Similarly, Salisu et al. (2025) applied response surface methodology (RSM) and a genetic algorithm–assisted artificial neural network (ANN–GA) for rice husk–plastic co-gasification, with ANN–GA outperforming other models ($R^2 > 0.99$) in both prediction and optimization [39]. Yang et al. (2023) trained Gradient Boosting Regressor models for MSW gasification to predict char, tar, gas yields, and syngas composition, further applying SHAP analysis to identify the most influential input features [40].

Despite their accuracy, ML models often suffer from limited interpretability, a challenge known as the “black-box problem” [41]. In the thermochemical process, it is crucial to understand why a particular prediction is made and how input parameters influence the process. To address this, several recent studies have integrated explainable AI methods such as SHAP and PDP. For instance, Xue et al. (2024) employed SHAP and PDP analyses to interpret ML models predicting syngas composition in BFBG, identifying specific process variables as the most influential input parameters [42]. Similarly, Khandelwal et al. (2025) utilized SHAP analysis to predict hydrogen yield from supercritical water gasification, concluding that temperature is the predominant influential feature [43]. Pandey et al. (2023) further developed explainable ML models specifically for BFBG processes, employing SHAP analysis to explain global feature contributions to prediction [44]. Additionally, Vaiyapuri et al. (2025) optimized H_2 production in co-

gasification using diverse ML models and conducted interpretability analyses at both global and local scales using SHAP summary and force plots, significantly enhancing model transparency [45].

1.3. Research gap and objectives

A thorough review of the literature reveals that most existing studies on biomass and waste gasification adopt individual modeling strategies like equilibrium models, kinetic models, or ML approaches. However, comparative analyses across these different modeling strategies remain notably sparse, limiting the understanding of their relative accuracy and reliability in representing experimental outcomes. This creates a critical research gap, the lack of a systematic, experimentally grounded comparison across modeling paradigms for diverse feedstock co-gasification in BFBG.

The present study addresses this gap by compiling an extensive and carefully constrained dataset from published experiments involving steam and steam–O_2 co-gasification of lignocellulosic biomass, MSW, plastic waste, and their combinations. This data set provides a robust foundation for conducting a rigorous comparative evaluation of equilibrium and kinetic models implemented in Aspen Plus alongside surrogate ML models. By directly benchmarking predictions against experimental results, the study identifies the most accurate and robust framework for predicting syngas composition. The distinctive and novel contributions of this work are outlined as follows.

1. This study presents an extensive comparative evaluation of conventional first-principle based and ML models for co-gasification in BFBG. The analysis is based on a curated dataset designed to minimize external variability.
2. ML models are developed to explicitly incorporate BFBG configuration, feedstock characteristics, and operating variables. Multiple algorithms are systematically screened to identify the most effective predictive framework.
3. To further strengthen model reliability, synthetic data is generated using a cGAN. In addition, explainable artificial intelligence methods, namely SHAP and PDP, are employed to identify key process drivers. Together, these strategies enhance both the robustness and interpretability of ML predictions.

In this article, Section 2 presents the methodology, including data collection, modeling frameworks, and performance evaluation criteria. Section 3 reports the results and offers a detailed discussion of model comparisons and interpretability analyses. Finally, Section 4 summarizes the key conclusions and presents prospects for future work.

2. Methodology

This study adopts a systematic modeling framework for the robust prediction of syngas composition from the steam co-gasification of biomass and waste in BFBG. The methodology begins with the curation of a comprehensive experimental database, compiled through a rigorous bibliographic review of studies focused on BFBG systems employing steam and steam–O_2 as gasifying agents. This dataset serves as the foundation for two modeling strategies: (i) first-principles simulations, including TEM, RTM, and KM developed in Aspen Plus; and (ii) data-driven surrogate modeling using suite of ML regressors was trained and benchmarked against the experimental data. Top performing ML model and first-principle models' outputs were evaluated based on their predictive performance. Additionally, a cGAN was implemented to generate synthetic data conditioned on process inputs, supporting subsequent sensitivity analyses. Finally, the trained ML models were subjected to explainability analyses using SHAP and PDPs, providing deeper insights into the influence of process variables on syngas composition.

2.1. Data preparation

The dataset was carefully prepared to ensure both quality and relevance for subsequent analysis. This process began with a systematic collection of experimental data on steam and steam–O_2 co-gasification through an extensive review of Scopus and the Web of Science databases. To ensure methodological consistency, only studies conducted in BFBGs were considered. Further inclusion criteria required that each publication report: (i) gasification experiments involving municipal solid waste, plastic waste, or lignocellulosic biomass under steam or steam–O_2 atmospheres; (ii) complete feedstock characterization; (iii) explicit details of reactor configuration (diameter and height); and (iv) syngas composition expressed in molar or volume percentages. Applying these stringent filters yielded 20 eligible articles, from which 214 experimental samples were extracted.

The collected dataset was subsequently refined through a rigorous preprocessing protocol, including the identification and removal of outliers, verification of data consistency, and correlation analysis of key process variables. These quality-assurance measures ensured the robustness and reliability of the dataset, providing a solid foundation for the subsequent modeling framework. A full listing of the selected studies, along with feedstock types and experimental conditions, is provided in Table S1, while the complete dataset is available in the Supplementary Excel file.

The final dataset comprises 12 input variables that collectively capture reactor geometry, feedstock properties, and operating conditions. Reactor geometry is represented by diameter (D, cm) and height (H, cm). Feedstock composition, given in weight percentage (wt%), include ash content (Ash), fixed carbon (FC), volatile matter (V), and elemental composition (H, C, O). Operating parameters encompass gasification temperature (T, (°C)), feedstock flowrate (kg/h), steam-to-biomass ratio (S:B), and equivalence ratio (ER). The output variables of interest are the mole percentage (mol %) of H_2, CO, CO_2, and CH_4. A statistical summary of the input features is presented in Table S2, while Table S3 details the observed ranges and mean values of the syngas components across all experiments. This carefully curated dataset forms the basis for the comparative modeling and analysis of syngas composition in BFBG gasification processes.

2.2. Models from process simulators

All gasification simulations were conducted in Aspen Plus V14.0, employing both equilibrium and kinetic modeling strategies in accordance with Ajorloo et al. (2017) [31]. Biomass, char, and ash were treated as nonconventional components, with their proximate and ultimate analyses specified through ULTANAL and PROXANAL property options. Thermodynamic properties of the gaseous species were sourced from the Aspen Plus database, while enthalpies and densities were computed using HCOALGEN and DCOALIGT correlations. The Peng–Robinson equation of state, combined with Boston–Mathias modifications, was employed to describe the system thermodynamics [46].

2.2.1. Equilibrium modeling

Equilibrium modeling of biomass gasification can be implemented through two principal approaches which are RTM and TEM. RTM relies on a predefined set of chemical reactions to describe the conversion of biomass into syngas. By tracking species through a stoichiometric reaction network, it provides detailed mass and energy balances that capture the influence of key reactions on syngas composition. In contrast, TEM does not depend on explicit reaction pathways. Instead, it determines the equilibrium state by minimizing the Gibbs free energy of the system, requiring only the elemental composition of the feedstock (from ultimate analysis) and operating conditions such as temperature and pressure. This makes TEM computationally efficient and particularly useful for rapid preliminary assessments.

While both methods are widely applied, they share certain

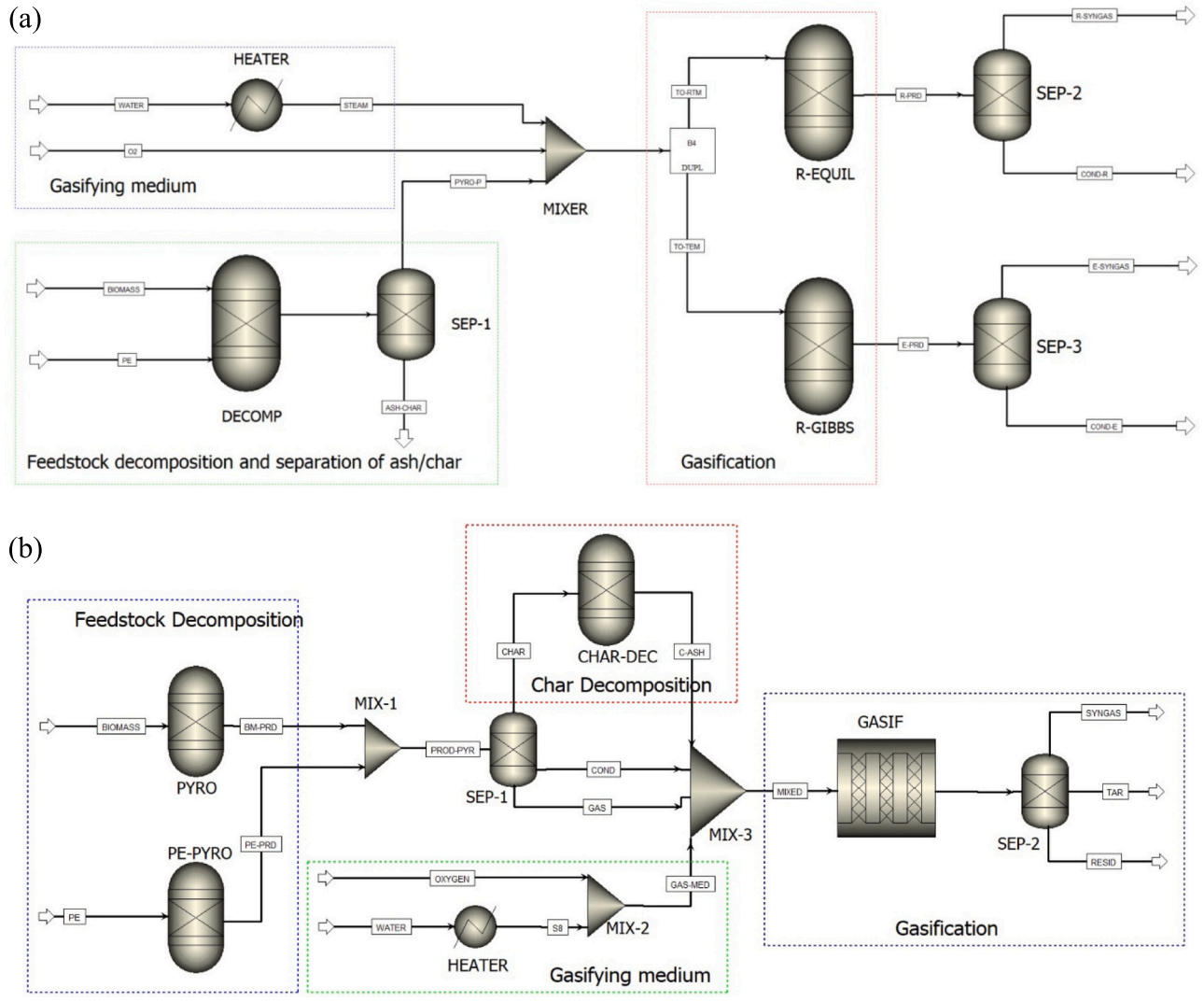

Fig. 1. Process flow sheet (a) equilibrium model (b) kinetic model.

Table 1
Steam gasification reactions considered [48].

Type		Reaction	ΔH_r° (kJ/mol)
Carbon Reactions	R1	$C + CO_2 \rightarrow 2CO$	172
	R2	$C + H_2O \rightarrow CO + H_2$	131
	R3	$C + 2H_2 \rightarrow CH_4$	−74.8
	R4	$C + 0.5O_2 \rightarrow CO$	−111
	R5	$C + O_2 \rightarrow CO_2$	−394
Oxidation Reactions	R6	$CO + 0.5O_2 \rightarrow CO_2$	−284
	R7	$CH_4 + 2O_2 \rightarrow CO_2 + 2H_2O$	−803
	R8	$H_2 + 0.5O_2 \rightarrow H_2O$	−242
Shift Reaction	R9	$CO + H_2O \rightarrow CO_2 + H_2$	−41.2
Methanation Reactions	R10	$CO + 2H_2 \rightarrow CH_4 + H_2O$	−247
	R11	$CO_2 + 4H_2 \rightarrow CH_4 + 2H_2O$	−206
Steam-Reforming Reactions	R12	$CH_4 + H_2O \rightarrow CO + 3H_2$	206
	R13	$CH_4 + 0.5O_2 \rightarrow CO + 2H_2$	−36
Methanation Reactions	R14	$CO + 3H_2 \rightarrow CH_4 + H_2O$	−165

limitations. Neither TEM nor RTM accounts for kinetic barriers, reactor hydrodynamics, or secondary chemistry such as char and tar formation. As a result, they often overpredict hydrogen and carbon monoxide yields while underestimating carbon dioxide and methane. Moreover, because equilibrium is assumed to be fully achieved, these models cannot capture the effects of reactor geometry or residence time, restricting their utility for detailed design or scale-up studies. RTM addresses part of this gap by introducing adjustable parameters in the form of approach temperatures for specific reactions, thereby offering a more realistic representation of gasification behavior under practical conditions.

Unlike TEM, which assumes that all reactions proceed to full equilibrium, RTM explicitly acknowledges that gasification processes are often constrained by kinetic and operational limitations. By introducing approach temperatures that shift reaction equilibria away from the reactor's actual operating point, RTM provides a more realistic representation of gasification behavior. This adjustment improves the accuracy of syngas composition predictions and enhances the reliability of performance indicators, which is particularly important for biomass air gasification where deviations from ideal equilibrium are significant.

In this study, both TEM and RTM simulations were implemented in Aspen Plus following the framework of Acar et al. (2019) [47]. The process flowsheet is shown in Fig. 1 (a). Biomass or plastic waste is first decomposed in an RYIELD reactor (block ID: DECOMP) into its elemental constituents based on proximate and ultimate analyses. Ash, defined as an inert fraction, is removed using a separator (SEP1). The elemental streams are then combined in a mixer (MIX1) and directed to the gasifier. TEM is represented by an RGIBBS reactor (R-GIBBS), which minimizes Gibbs free energy, while RTM is represented by an REQUIL reactor (R-EQUIL), where equilibrium constraints are applied selectively. Syngas is subsequently isolated from the product stream through separators (SEP2 and SEP3). A detailed description of the process blocks

is provided in Table S4.

Both TEM and RTM simulations were developed under the following assumptions: (i) ash is inert; (ii) the system operates under steady-state conditions; (iii) NH_3 and H_2S are excluded; (iv) tar formation is neglected; and (v) heat losses and pressure drops are considered negligible. These simplifying assumptions are consistent with prior studies and ensure comparability with the existing literature.

The validity of the RTM framework has been demonstrated in earlier works. Abdelrahim et al. (2020), for instance, showed that calibration of approach temperatures significantly improved agreement with experimental results [30]. Similarly, Acar et al. (2019) modeled BFBG gasification by restricting equilibrium in four key reactions (R2, R4, R9, R12; see Table 1) [47]. Following this precedent, the present study adopted the same reaction set and performed a targeted sensitivity analysis to identify the optimal approach temperature for each reaction. From Table 1, for R9 (water–gas shift), the restricted temperature was varied between 0 °C and 1000 °C, while for R12 (methane steam reforming), it was varied between 0 °C and − 500 °C. Sensitivity trials indicated that variations in R2 and R4 had negligible influence on syngas composition, so their approach temperatures were fixed at 0 °C.

This calibration was applied iteratively across the full dataset of 208 experimental samples. For each case, the approach temperatures were tuned to minimize deviations between predicted and measured syngas compositions, as quantified by the error function in eq. 1 [21].

$$\begin{aligned}(\text{Minimum error})_i = &\left| {H_2}^{exp} - {H_2}^{pred} \right|_i + \left| {CO}^{exp} - {CO}^{pred} \right|_i \\ &+ \left| {CO_2}^{exp} - {CO_2}^{pred} \right|_i + \left| {CH_4}^{exp} - {CH_4}^{pred} \right|_i \end{aligned} \quad (1)$$

2.2.2. Kinetic modeling

The kinetic model (KM) was developed in Aspen Plus to simulate the co-gasification of biomass, municipal solid waste, and plastic waste under realistic thermochemical conditions. Unlike equilibrium-based models, which assume ideal conversion, the KM explicitly incorporates reaction kinetics, thereby accounting for rate limitations imposed by temperature, pressure, residence time, and reactor configuration. This enables a more mechanistic and physically grounded representation of the BFBG process. The overall process flow sheet is shown in Fig. 1 (b), with a description of the model blocks provided in Table S5.

Biomass and plastic feedstocks were first decomposed in an RYield unit. For biomass (block ID: PYRO), decomposition kinetics followed the empirical correlations of Neves et al. (2011) [49], which are widely validated for lignocellulosic materials. In contrast, plastic waste decomposition (block ID: PE-PYRO) was represented using proximate and ultimate analyses to capture its distinctive pyrolytic behavior. Under high-temperature conditions, plastics undergo primary depolymerization of long polymer chains, followed by secondary cracking of the resulting char, consistent with reported mechanistic pathways [50]. The decomposition products were then separated in a SEP2 column into gases, condensable, and char. Char was further decomposed in an additional RYield reactor (block ID: CHAR-DEC) into elemental carbon, sulphur (where present in the feedstock), and ash.

All decomposition products, together with the gasifying agent, were subsequently combined in a mixer (block ID: MIX2) and introduced into a plug flow reactor (PFR) to model the gasification stage. The PFR configuration was chosen to approximate the hydrodynamics of a bubbling fluidized bed, where axial gradients in concentration and temperature significantly affect conversion. Within the PFR, the pyrolysis products react with the gasifying medium to yield syngas, tar, and residual solids. Reaction rates were defined using experimentally calibrated Arrhenius-type rate equations, with kinetic parameters obtained from the literature. The kinetic datasets employed are summarized in Tables S6 and S7. The KM is based on the following assumptions:

1. Ash is treated as inert and classified as nonconventional.
2. Heat losses and pressure drops are neglected.
3. Nitrogen-containing (NH_3) and sulphur-containing (H_2S) species are excluded from the reaction network.
4. Tar compounds (C_6H_6O, C_6H_6, $C_{10}H_8$) are included in the mechanism but excluded from result reporting to maintain focus on syngas.
5. All rate expressions follow the Arrhenius form.

2.3. Surrogate modeling and explainable ML

In this study, a preliminary screening of ML regression models was implemented to evaluate the applicability of data-driven approaches for syngas composition prediction. These ML models included random forest (RF), extra trees (ET), k-Nearest Neighbors (kNN), Extreme Gradient Boosting (XGB), Support Vector Regression (SVR) and Neural Network (NN). A brief overview of the models employed in this study is available in the supplementary material. To ensure a fair performance comparison, each model was assessed using the same input-output dataset using a 10-fold cross-validation technique. All input components were normalized to zero mean and unit variance using Scikitlearn's StandardScaler before the model was trained. All models were subjected to the same preprocessing pipeline. Each of these models was systematically tuned using the Optuna optimization framework to ensure optimal performance.

2.3.1. ML models performance

This section focuses on evaluating the performance of the ML models to determine their ability to predict syngas composition values based on the proposed input features. A brief overview of the techniques employed in this study is available in the supplementary material. To assess the predictive accuracy and reliability of the surrogate models, multiple performance metrics were calculated for both training and testing datasets. These metrics are the coefficient of determination (R^2), the RMSE, and the mean square error (MSE).

The R^2 score measures the proportion of variance in the target variable that is explained by the model. Provides a relative measure of fit goodness, with values ranging from perfect fit, $R^2 = 1$, to poor fit, $R^2 = 0$. Mathematically, it is defined as in the following equation where y_i is the observed value, $\hat{y}_i$ is the predicted value, $\bar{y}_i$ is the mean of the observed values, and n is the number of data points.

$$y^2 = 1 - \frac{\sum_{i=1}^{n} (y_i - \hat{y}_i)^2}{\sum_{i=1}^{n} (y_i - \bar{y}_i)^2} \quad (2)$$

The RMSE represents the square root of the average squared differences between predicted and observed values. It penalizes larger errors more heavily, making it sensitive to outliers. The formula is as follows.

$$RMSE = \sqrt{\frac{1}{n} \sum_{i=1}^{n} (y_i - \hat{y}_i)^2} \quad (3)$$

The MSE measures the average squared difference between the predicted values and the actual values in a dataset. It quantifies how close a model's predictions are to the true values.

$$MSE = \frac{1}{n} \sum_{i=1}^{n} (y_i - \hat{y}_i)^2 \quad (4)$$

2.3.2. Synthetic data generation

To support a robust interpretability analysis of the ML models, a cGAN was employed to generate high-quality synthetic data, addressing the limitations of the small experimental dataset. GANs are a class of generative models comprising two competing neural networks: a generator G, which learns to produce synthetic data resembling the true data distribution, and a discriminator D, which attempts to distinguish between real samples (from the actual data distribution) and fake samples (generated by G) [51]. In a cGAN, both G and D receive

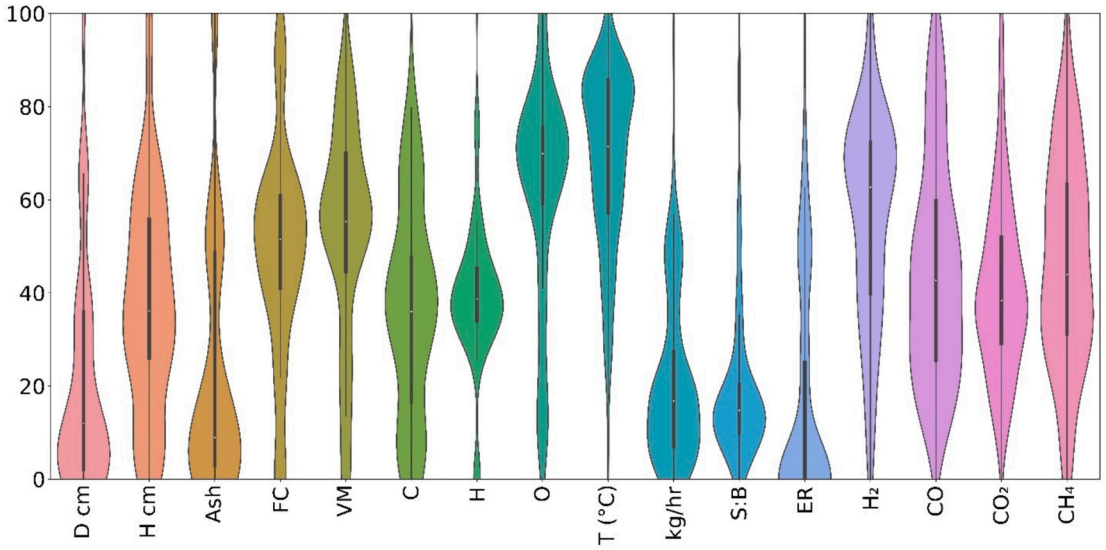

Fig. 2. Data distribution of inputs and outputs.

additional input information, referred to as the condition *c*, which can be a vector of known variables or features. This enables the model to generate data samples conditioned on specific input features, allowing greater control over the output distribution [52]. In this study, the original dataset, comprising experimentally measured feedstock and corresponding syngas compositions, was first normalized using Min-Max scaling. The cGAN was implemented in PyTorch, where the generator *G (z,c)* takes a random latent vector $z \sim N(0,I)$ and a condition vector *c* (i.e., the known input features) and maps them to a synthetic output sample. The discriminator *D(x,c)* then receives either a real data sample *x* or a generated one *G(z,c)*, along with the same condition *c*, and predicts whether the input is real or synthetic.

The networks were trained in an adversarial setup using the binary cross-entropy loss function. The objective functions are given as:

$$\mathscr{L}_D = -E_{x\sim Pdata}[\log D(x,c)] - E_{z\sim N(0,I)}\left[\log\left(1 - D(G(z,c),c)\right)\right] \quad (5)$$

$$\mathscr{L}_G = -E_{z\sim N(0,I)}\left[\log\left(1 - D(G(z,c),c)\right)\right] \quad (6)$$

These objectives ensure that the generator learns to produce data *G (z,c)* that the discriminator cannot reliably distinguish from real samples, thereby minimizing the divergence between real and synthetic data distributions. Both networks were implemented using specifically MLPs which are capable of learning complex, non-linear mappings due to their layered architecture of non-linear activation functions. To further improve the diversity and fidelity of the generated samples, a Maximum Mean Discrepancy (MMD) regularization term was incorporated into the generator's loss function. MMD measures the discrepancy between real and generated data distributions in a high-dimensional feature space. Therefore, the final loss for the generator was calculated as a weighted sum of the adversarial loss and the MMD penalty. This combined approach encourages the generator not only to fool the discriminator, but also to produce statistically coherent samples that align with the true data distribution.

Importantly, the synthetic data generated by the trained cGAN was not used to train predictive models. Instead, it was used as an extended dataset to enable richer post hoc interpretability analysis (e.g. SHAP, PDP) under a broader range of input conditions. While previous works, such as Ganguly et al. (2022), have utilized GANs for augmenting feedstock variability in pyrolysis systems [53]. To the best of the authors' knowledge, this is the first application of a cGAN to generate synthetic data for steam co-gasification processes.

The model was trained for two thousand epochs with batch-wise updates to both the generator and discriminator using the Adam optimizer. Label smoothing and noise were added to the real and fake labels, respectively, to mitigate overconfidence and stabilize convergence. Upon completion, the trained generator was used to synthesize three thousand new samples by sampling latent vectors and randomly selected condition vectors from the real dataset. Post-processing constraints were applied to ensure the physical and chemical validity of the synthetic samples. Proximate analysis VM, FC, Ash, and moisture content were normalized to ensure their sum equaled 100 %. Elemental ash content from proximate analysis was calculated by subtracting the sum of major elements (C, H, and O) from 100. Additionally, syngas component concentrations (H_2, CO, CO_2, CH_4) were normalized to unity to preserve mass balance. Values below a practical threshold (e.g., ER < 0.01) were clamped to zero and all negative values were removed to eliminate nonphysical outputs.

2.3.3. ML model interpretability

While ML models often achieve strong predictive performance, their internal intricacies can obscure the reasons behind individual predictions. To improve transparency and make the models more interpretable for practical use, this study incorporates two widely used techniques: SHapley Additive exPlanations (SHAP) and Partial Dependence Plots (PDPs).

SHAP, originally proposed by Lundberg and Lee, [54], is based on cooperative game theory and assigns each feature a quantitative contribution to model predictions [55]. As a member of the broader class of additive feature attribution methods, SHAP maintains a model-agnostic nature, allowing its application across a wide range of ML algorithms. This makes it a powerful tool to explain the importance of features and to enhance the interpretability of complex models. Mathematically, SHAP values are computed by evaluating the change in model prediction when a feature is included versus excluded from a subset of features, repeated across all feature combinations. This ensures consistency and fairness in the assignment of prediction responsibility. An explanatory model ζ is given by eq. 7.

$$\zeta(x) = \phi_o + \sum_{i=1}^{M} \phi_i Y_i' \quad (7)$$

Here $Y_i' \in \{0,1\}^M$, specifies the subset of *M* attributes contributing to the decision for instance *i*. The SHAP contribution ϕ_i of feature *i* for a given sample is computed by eq. 8.

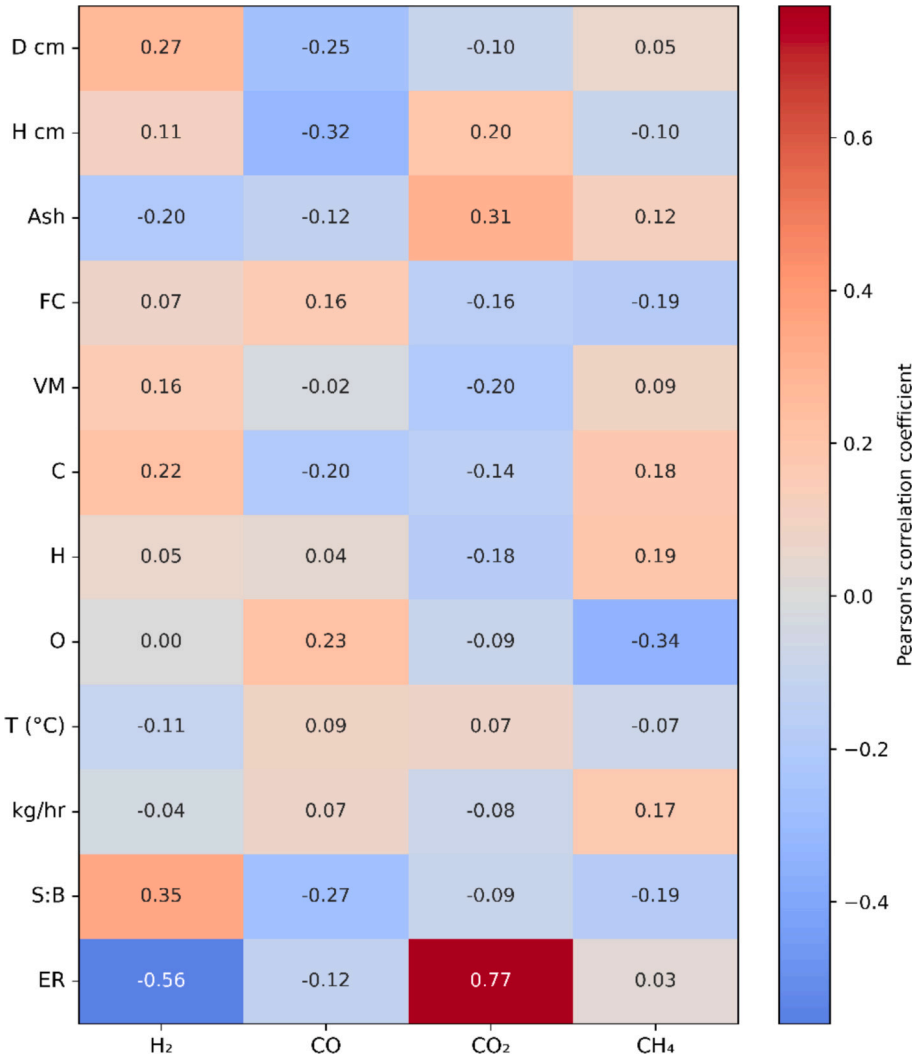

Fig. 3. Pearson's correlation matrix.

$$\phi_i = \sum_{G \subseteq N\{i\}} \frac{|G|!(M-|G|-1)!}{M!} [f_x(G \cup \{i\}) - f_x(G)] \tag{8}$$

Where N refers to the entire feature space comprising M attributes, and G indicates the selected subset of those attributes, of size $|G|$.

PDPs, originally introduced by Friedman, are global interpretability tools that visualize the average effect of one or two input features on the predicted output, while marginalizing over the influence of all other features [56]. The PDP function estimates the expected model response when a selected input variable is fixed at a given value and all other variables vary across their distributions. This provides a broader understanding of the model sensitivity and response trends in the input space. Formally, the partial dependence of a target function f on a selected subset of features x_S is defined as:

$$f_S(x_S) = \int f(x_S, x_C) dP(x_C) \tag{9}$$

Where x_S are the features of interest and x_C denotes the complementary set of features. The integration is performed over the marginal distribution $P(x_C)$ of the remaining features.

3. Results and discussion

3.1. Data analysis

The distribution of the twelve input and four output features is illustrated in Fig. 2, where the width of each violin reflects the density of the data. To enable a consistent comparison across variables with different magnitudes and units, all features were normalized using Min–Max scaling and expressed on a common scale ranging from 0 to 100. This normalization ensures that variations in distribution are attributed to the inherent behavior of the variables rather than their original measurement scales. The descriptive statistics of the input features are summarized in Table S2, while Table S3 provides the corresponding statistical characteristics for the output features, including their ranges, mean values, and standard deviations.

The Pearson correlation matrix, presented in Fig. 3, highlights the relationships between the input variables and the output variables, providing insights into the dependencies among them. For H_2 production, ER plays a significant role, showing a strong negative correlation, indicating that higher levels suppress H_2 yields. Conversely, other inputs such as S:B and D cm, exhibit positive impact on the yield of H_2. CO production, however, is positively influenced by FC, O, and kg/h. whereas S:B and ER have inverse relationship, highlighting its slight inhibitory effect on CO levels.

Table 2
R^2, RMSE, and MSE for syngas based on train and test (given in parentheses) data.

		RF	ET	kNN	XGB	SVR	NN
H_2	R^2	0.9639 (0.8365)	0.9827 (0.8549)	0.9820 (0.8198)	0.9716 (0.871)	0.9561 (0.8851)	0.965 (0.878)
	RMSE	0.1898 (0.3803)	0.1311 (0.3528)	0.1339 (0.4048)	0.0187 (0.0376)	0.2093 (0.3243)	0.0206 (0.0366)
	MSE	0.0361 (0.1601)	0.0173 (0.1401)	0.018 (0.1735)	0.0003 (0.0015)	0.0439 (0.1133)	0.0004 (0.0014)
CO	R^2	0.9114 (0.7875)	0.98 (0.8434)	0.987 (0.8161)	0.9699 (0.8758)	0.9606 (0.8771)	0.974 (0.873)
	RMSE	0.2973 (0.4307)	0.1409 (0.3645)	0.1131 (0.3988)	0.016 (0.03)	0.1981 (0.3221)	0.0147 (0.0303)
	MSE	0.0885 (0.1931)	0.02 (0.1457)	0.013 (0.1715)	0.0003 (0.001)	0.0393 (0.111)	0.0002 (0.001)
CO_2	R^2	0.974 (0.8273)	0.9701 (0.8268)	0.9921 (0.8225)	0.9562 (0.8545)	0.9461 (0.8836)	0.961 (0.858)
	RMSE	0.1610 (0.3791)	0.1722 (0.3778)	0.0886 (0.3863)	0.0188 (0.0314)	0.1981 (0.3221)	0.0176 (0.03)
	MSE	0.026 (0.1621)	0.03 (0.1601)	0.0079 (0.1709)	0.0004 (0.0011)	0.054 (0.1144)	0.0003 (0.001)
CH_4	R^2	0.9151 (0.7443)	0.9205 (0.7355)	0.9798 (0.7469)	0.9144 (0.7723)	0.9431 (0.8043)	0.938 (0.822)
	RMSE	0.2909 (0.4631)	0.2816 (0.4657)	0.1404 (0.4601)	0.0108 (0.0162)	0.2379 (0.3983)	0.009 (0.0146)
	MSE	0.0848 (0.2242)	0.0794 (0.2311)	0.0201 (0.2229)	0.0001 (0.0003)	0.0568 (0.1677)	0.0001 (0.0001)

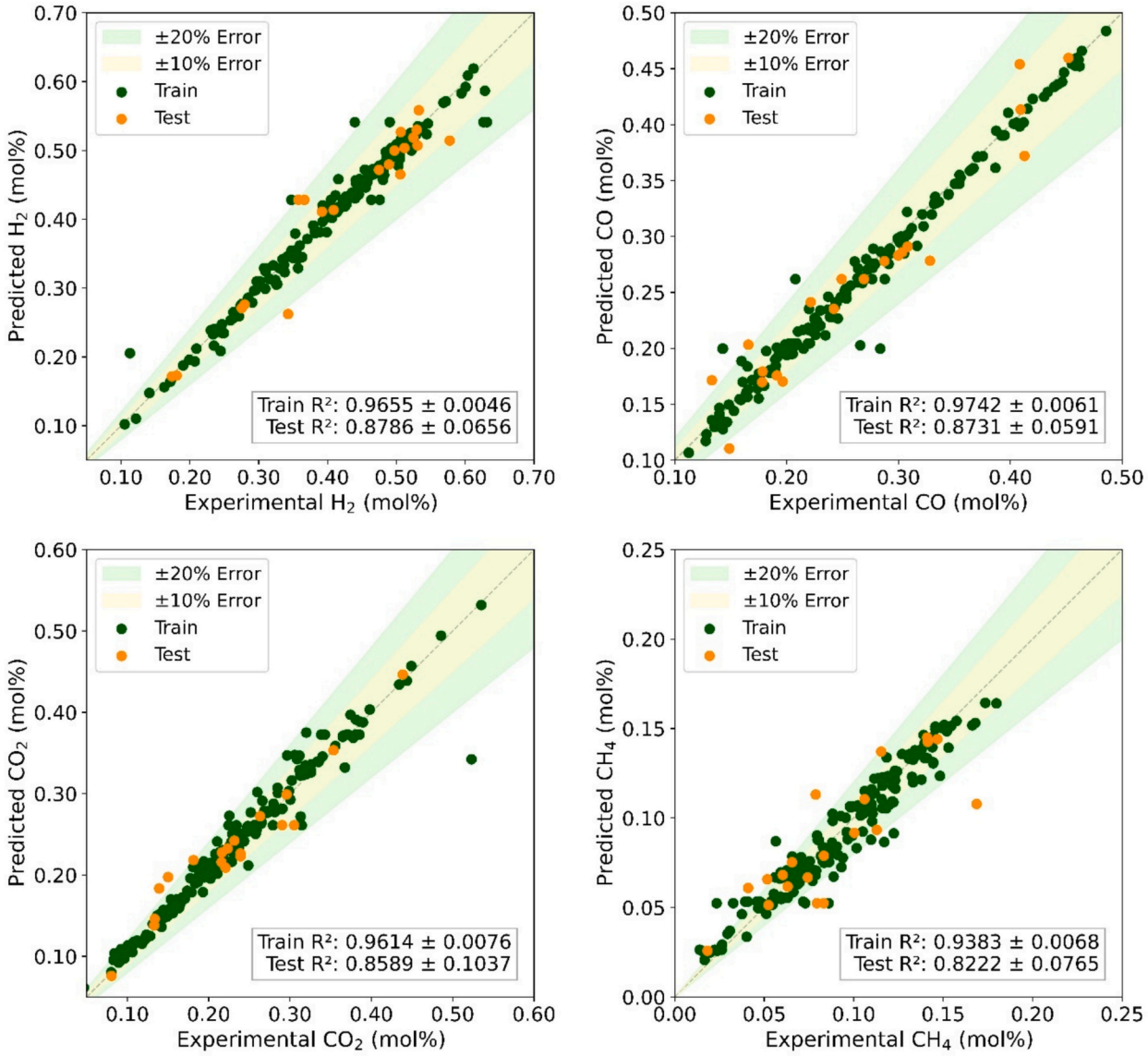

Fig. 4. Scatter plot for the prediction performance for all the syngas

CO_2 production demonstrates a strong dependence on ER, with a high positive correlation with ER, highlighting its critical role in optimizing CO_2 yields. CH_4 production follows a different trend, with C and VM showing positive correlation. O and S:B have the most negative impact on the yield of CH_4 in syngas. Overall, D cm, H cm, FC, T (°C), S:B, and ER stand out as key variables for optimizing H_2, CO, and CO_2 production, while methane appears less sensitive to the selected inputs, suggesting the need to explore additional factors for its optimization.

To ensure that the dataset, carefully curated with systematic criteria, was suitable for subsequent modeling, outlier detection was performed using two robust statistical approaches: IQR method based on the covariance-driven Mahalanobis distance and the kNN technique. A total

Table 3
RMSE values for the different modeling techniques.

		RTM	TEM	KM	NN
H_2	MSE	0.01396	0.04845	0.02993	0.00049
	RMSE	0.11814	0.22011	0.17300	0.02204
CO	MSE	0.01158	0.02137	0.04466	0.00025
	RMSE	0.10759	0.14619	0.21132	0.01589
CO_2	MSE	0.00918	0.01508	0.01600	0.00040
	RMSE	0.09580	0.12281	0.12648	0.02008
CH_4	MSE	0.00425	0.00983	0.00163	0.00013
	RMSE	0.06519	0.09915	0.04039	0.01160
Average	MSE	0.00974	0.02368	0.02305	0.00032
	RMSE	0.09668	0.14707	0.13780	0.01740

of five outliers were identified using the IQR method. Among these, three were independently confirmed by the kNN approach, indicating consistency across the methods. The distribution of outliers detected by the IQR method is illustrated in Fig. S1, while Fig. S2 and Fig. S3 present the parameter tuning process involved in the detection of outliers based on kNN. For ease of identification, the corresponding outliers are highlighted in red in the supplementary Excel file.

3.2. ML model development and hyperparameter optimization

The ML algorithms were implemented to evaluate their performance in predicting four target outputs: H_2, CO, CO_2, and CH_4. Each ML model was optimized individually by output using Optuna-based optimization for optimal architecture and hyperparameters. As shown in Table 2, each model's performance was measured through R^2, RMSE, and MSE, both for training and test datasets (values in parentheses). Table S8 shows the optimized hyperparameter for each ML model for every output.

For H_2 prediction, RF, ET, and kNN exhibited the lowest predictive accuracy, with kNN achieving the weakest test R^2 score of 0.8198, along with the highest RMSE (0.4048) and MSE (0.1735). In contrast, XGB and SVR demonstrated stronger performance, attaining test R^2 values of 0.871 and 0.8851, respectively. However, XGB notably outperformed SVR in terms of generalization, with significantly lower RMSE (0.0376) and MSE (0.0015). Similarly, the NN achieved excellent results, with training and test R^2 values of 0.965 and 0.878, respectively. The low RMSE (0.0366) and MSE (0.0014) of the model further highlight its strong generalizability in predicting H_2. Similarly, in the case of CO, RF again produced the lowest performance, while ET and kNN performed moderately better in terms of R^2 but showed high RMSE and MSE, suggesting considerable overfitting. On the contrary, SVR achieved the highest test R^2 (0.8771), its high error metrics (RMSE: 0.3221; MSE: 0.111) indicated poor generalization. On the other hand, both XGB and NN performed consistently well, with test R^2 values of 0.8758 and 0.873, respectively. Notably, NN achieved the lowest RMSE (0.0303) and MSE (0.0002), confirming its effective predictive capability and stability for CO prediction.

For CO_2, RF, ET, and kNN again lagged in performance, with low R^2 values and elevated RMSE and MSE scores. Although SVR achieved a solid test R^2 of 0.8836, its error metrics remained high, limiting its overall reliability. In contrast, XGB and NN demonstrated robust performance, both achieving high R^2 values and the lowest RMSE and MSE scores across folds, affirming their strong generalization capabilities for CO_2. CH_4 posed a greater challenge, as most algorithms, except SVR and NN, yielded test R^2 scores below 0.80, indicating poor predictive performance. SVR achieved a test R^2 of 0.8043, but its test RMSE (0.3983) and MSE (0.1677) were again higher. NN emerged as the best-performing model for CH_4 as well, with R^2 scores of 0.938 (train) and 0.822 (test), and the lowest test RMSE (0.0146) and MSE (0.0001), highlighting its robustness even for this complex output. Finally, NN was selected for further analysis and prediction of the syngas based on experimental data.

Fig. 4 shows the prediction performance of the NN ML model for all the syngas for the training and testing data, R^2 values are shown along with their standard deviation. The black line in the plots show the perfect predictions or ideal fit. The light-yellow shaded area shows the error interval of the 10 % in absolute values while the light green shaded portion shows an error interval of 10 %–20 %. The prediction performance comparison of the H_2, CO, and CO_2 concentration model after optimization shows that the points are close to the perfect fit line to the real values. It was found out that the distribution of points was more scattered in the case of CH_4 predictions, but most points were still distributed within the error interval of less than 10 %.

To evaluate the stability and generalization capacity of the optimized NN, learning curves were generated using 10-fold cross-validation and averaged for each syngas component: (a) H_2, (b) CO, (c) CO_2, and (d) CH_4. These curves, as shown in Fig. S4, plot the evolution of MSE loss for both training and validation datasets over three hundred epochs. Across all outputs, the learning curves exhibit a rapid initial decline in training and validation loss during the early epoch, indicating fast convergence and effective learning. As training progresses, the curves gradually flatten, signifying that the model reaches a stable optimization state.

3.3. Performance comparison: ML and process simulator models

Steam co-gasification in a BFBG was modeled using three approaches: TEM, RTM, and KM. A rigorous sensitivity analysis under the RTM scheme was then executed to adjust key parameters and closely replicate experimental syngas data. This analysis, performed using Aspen Plus's built-in sensitivity tools, primarily focused on the approach temperatures for each reaction. A total of 22,500 sensitivity instances were computed for each sensitivity analysis, and this analysis was performed for all 208 experimental cases. The absolute error was calculated for every instance, and the minimum absolute error was determined using eq. 1. The syngas composition corresponding to this minimum error was selected as the final RTM value. Similarly, the predictions from the NN were made on all the experimental data.

The RMSE and MSE values for different modeling strategies, RTM, TEM, KM, and NN, are presented in Table 3. These results highlight notable differences in the predictive performance of the models for co-gasification. The NN consistently outperformed all other models by a substantial margin across all outputs. For H_2, the NN achieved an RMSE of 0.022, compared to 0.118, 0.220, and 0.173 for RTM, TEM, and KM, respectively. This corresponds to a ~ 81 % improvement over the best-performing RTM model. Similar trends were observed for CO, where the NN reached an RMSE of 0.0159, an important reduction from the 0.107–0.211 range seen in the simulation models. For CO_2, the NN achieved an RMSE of 0.0201, again significantly lower than all baseline models (ranging from 0.0958 to 0.1265), indicating improved precision in capturing CO_2 behavior, which is often sensitive to equilibrium and kinetic assumptions. The greatest relative improvement was observed in CH_4 prediction, where the NN yielded an RMSE of 0.0116, outperforming even the best kinetic model (RMSE = 0.0404), with a ~ 71 % reduction in error.

In terms of average RMSE across all outputs, the NN attained 0.0174, while RTM, TEM, and KM exhibited significantly higher values of 0.0967, 0.1471, and 0.1378, respectively. This underscores the NN's exceptional capability to capture complex non-linear relationships in the process data, where conventional models, limited by idealized assumptions and simplified kinetics, fall short. Furthermore, the reduced MSE and RMSE indicate that NN predictions are not only closer to actual values but also more stable and less prone to variance across operating conditions.

The scatter plots in Fig. 5 compare the predictive performance of different modeling approaches for syngas composition, with ±10 % and ± 20 % error bands indicating prediction accuracy relative to experimental values. The predictions made by NN exhibit the highest degree of accuracy and consistency when compared to the experimental data. As

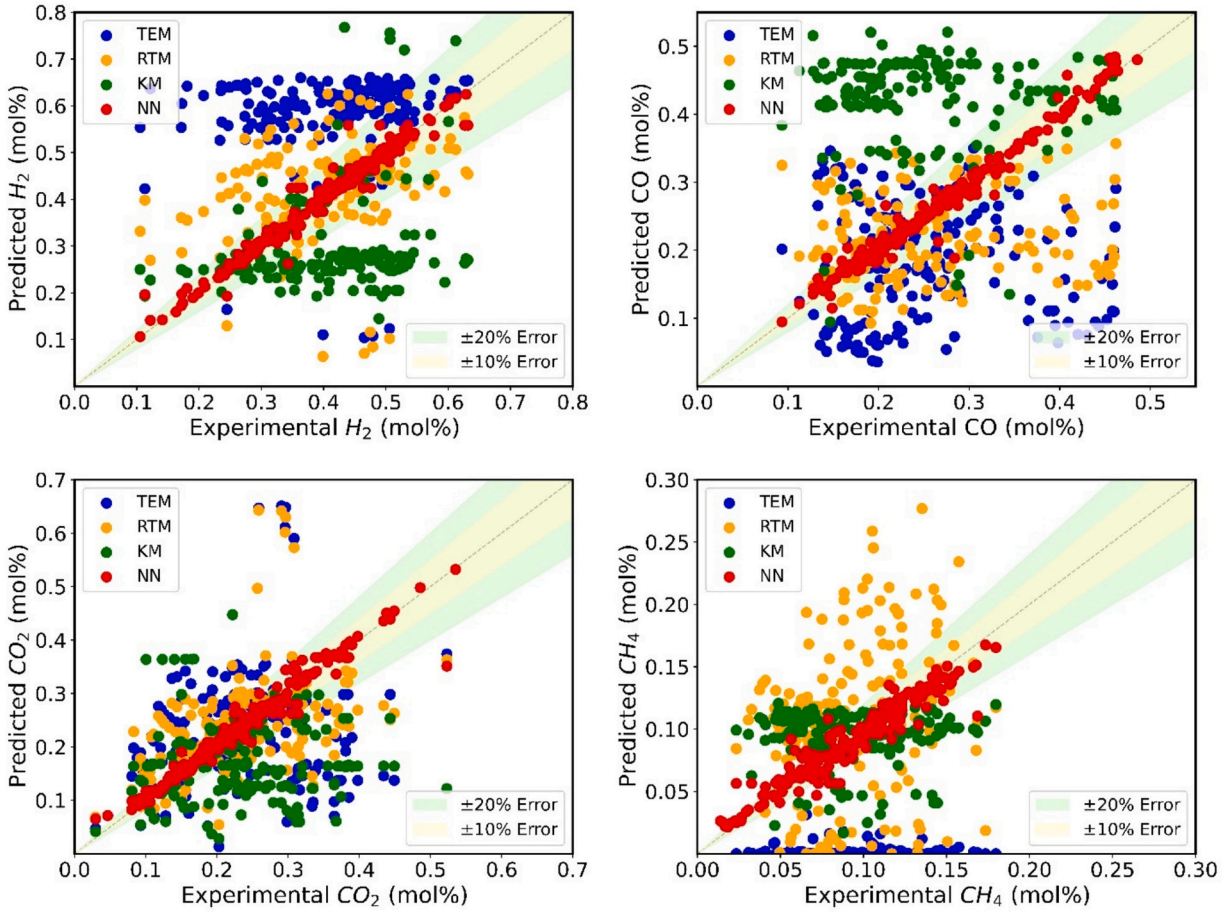

Fig. 5. Scatter plot between experimental and predicted values by different models.

Table 4
Comparative analysis of trend predictive efficiency of KM and NN models.

		Change in T (°C)								Change in S:B							
		H_2		CO		CO_2		CH_4		H_2		CO		CO_2		CH_4	
Names	Biomass	KM	NN	KM	NN	KM	NN	KM	NN	KM	NN	KM	NN	KM	NN	KM	NN
Yang et al.(2019) [58]	cotton stalk	+	+	−	−	−	−	−	−	+	+	−	−	+	+	−	−
Loha et al. (2011) [59]	rice husk	+	+	+	+	−	−	−	−	+	+	−	−	+	+	+	+
Nguyen et al. (2020) [60]	torrefied wood chips	+	+	−	−	+	+	−	−	+	+	−	−	+	+	−	−
Fremaux et al. (2015) [61]	wood residue	No data								+	+	−	−	+	+	+	+
Tuomi et al. (2015) [62]	wood	N/A								N/A							
	bark	N/A								N/A							
Pinto et al. (2016) [63]	rice husk, PE, rice straw	N/A								N/A							
Jeremiáš et al. (2014) [64]	wood	N/A								N/A							
Jeremiáš et al. (2017) [65]	wood	N/A								N/A							
Pecate et al. [66]	beech wood	−	−	+	+	+	+	**0**	**0**	+	+	−	−	+	+	−	−
Karmakar et al. [67]	rice husk	+	+	+	+	−	−	−	−	+	+	−	−	+	+	−	−
Pinto et al. (2002) [68]	pine	+	+	**0**	**0**	−	−	−	−	No data							
	90 % Pine +10 % PE	+	+	+	+	**0**	**0**	−	−	No data							
	60 % Pine +40 % PE	+	+	−	−	−	−	−	−	No data							
Herguido et al. (1992) [69]	pine	No data								+	+	−	−	+	+	−	−
Karatas et al. (2018) [70]	walnut shell	No data								+	+	−	−	+	+	−	−
	pistachio shell	No data								+	+	−	−	+	+	−	−
Masnadi et al. (2015) [71]	switch grass (spring)	N/A								N/A							
	switch grass (fall)	N/A								N/A							
Udomsirichakorn et al. (2013) [72]	pine	+	+	−	−	−	−	−	−	+	+	−	−	**0**	**0**	−	−
Brachi et al. (2014) [73]	Olive Husk + PET	N/A								N/A							
	Olive Husk + Tyre	N/A								N/A							
Miccio et al. (2009) [74]	Spruce wood	N/A								N/A							
Pinto et al. (2015) [75]	lignin	+	+	−	−	**0**	**0**	−	−	+	+	+	+	−	−	−	−
Jiang et al. (2024) [76]	Brewery spent grain	+	+	+	+	−	−	−	−	+	+	−	−	+	+	−	−

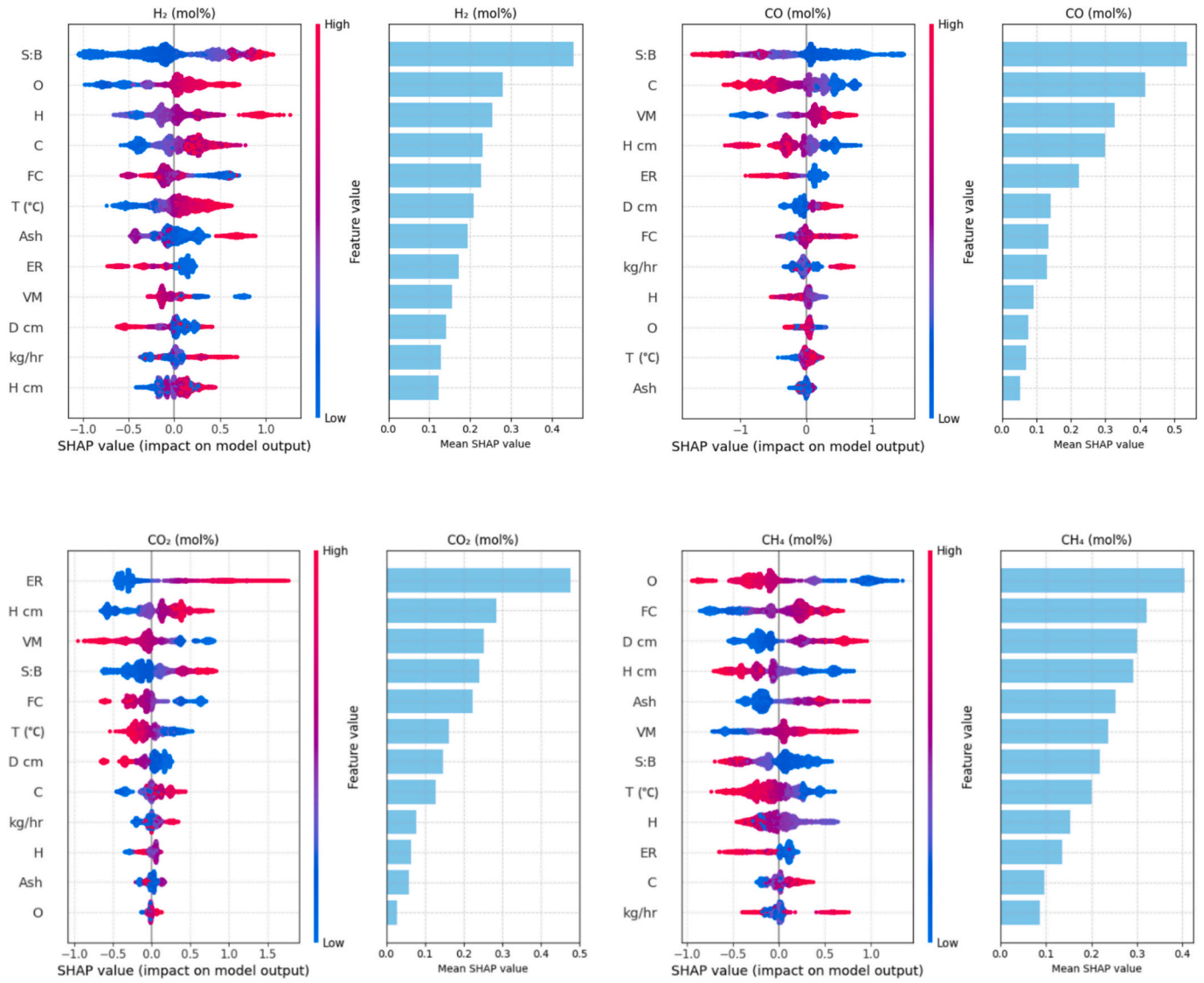

Fig. 6. Feature importance analysis and mean SHAP values of H_2, CO, CO_2, and CH_4.

highlighted by the close match between predicted and measured values and the minimal RMSE values in Table 3, this outcome is well supported. RTM, on the other hand, also displays good predictive accuracy for H_2, as evidenced by its scatter points clustering close to the predicted cluster of NN near to the perfect-fit line. However, its performance for other syngas components, particularly CH_4 and CO_2, indicates less robust generalizability. The scatter patterns for TEM reveal systematic over-prediction of H_2 and CO alongside underprediction of CO_2 and CH_4. Pilar et al. (2021) reported comparable error balancing, with excessive H_2 and CO estimates counteracted by corresponding deficits in CO_2 and CH_4 [57]. Such discrepancies highlight the limitations of TEM in effectively capturing the complexities of the co-gasification process, a shortcoming also evident from its higher RMSE values compared to NN and RTM.

Similarly, KM demonstrates modest predictive accuracy, with improvements over TEM for H_2 and CH_4. However, it predicts most poorly with CO and CO_2, where its predictions deviate significantly from the experimental values. This reinforces the notion that KM, like TEM, has inherent limitations in its modeling approach, particularly when addressing the intricate kinetics of co-gasification. These results highlight the significant performance differences among the models and the critical importance of selecting methodologies that align with specific reactor design. As KM relies heavily on kinetic parameters, derived from experiments that may vary across different reactor configurations and operational conditions, their reliance on fixed assumptions often limits their predictive accuracy. Such variations might also be attributable to differences in reactor configurations, which influence the underlying reaction kinetics.

In contrast, NN provides a compelling alternative by leveraging data-driven learning to model complex nonlinear relationships without being restricted by predefined kinetic assumptions. This flexibility allows NN to capture intricate dependencies between feedstock characteristics, reactor configuration, and operating variables, relationships that are challenging to encode explicitly in first-principle models. Accordingly, the findings of this study underscore the value of ML models, particularly NN, as an effective and efficient complement to conventional simulation frameworks for co-gasification studies. Residual analysis (Fig. S8) further corroborates these insights, with NN displaying the tightest alignment of predicted and experimental values across all syngas components.

Having established predictive performance, it is equally important to evaluate computational efficiency. All simulations were executed on a 9th generation Intel(R) Core(TM) i5–9500 CPU @ 3.00 GHz with 8 GB of RAM. The TEM required 24.1 s per run, the KM 2.60 s, and the RTM substantially longer, 13.89 min, due to its iterative sensitivity analysis framework. By comparison, NN training across all 10 folds required

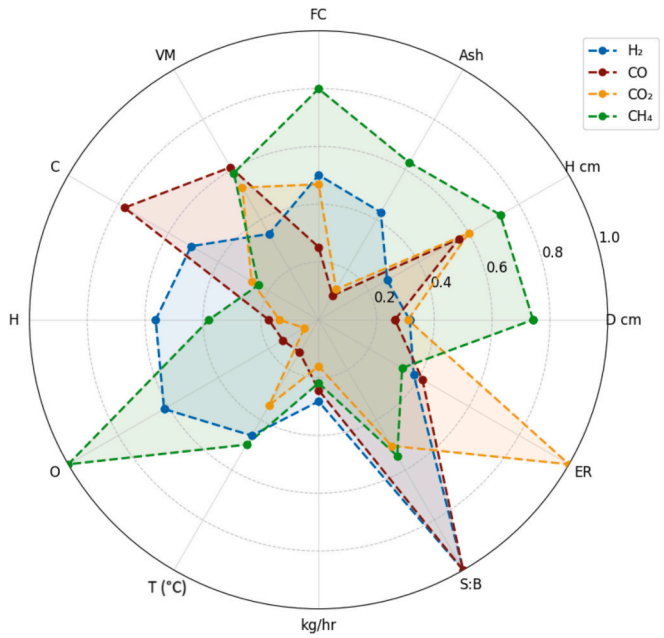

Fig. 7. Radar graph of the normalized SHAP feature importance analysis.

4.24 min; however, once trained, a single prediction required only 0.0442 s. This trade-off highlights the scalability of NN models: although training demands a moderate upfront cost, their near-instantaneous inference capability gives them highly suitable for integration into optimization workflows and potential real-time process control, where rapid decision-making is critical.

These models have also been qualitatively assessed against known experimental trends for selected input variables. Table 4 provides a comparative analysis of the experimental data trends predicted by the KM and NN models with respect to variations in temperature (T, °C) and steam-to-biomass ratio (S:B). In the experimental dataset, a plus sign (+) denotes an increasing trend, a minus sign (−) indicates a decreasing trend, and a zero (0) signifies no meaningful change in the corresponding syngas constituent. In a few experimental cases where T (°C) and S:B varied simultaneously, isolating the effect of either variable was not feasible; such instances are reported as not applicable (N/A) in Table 4. For model–experiment comparisons, green shading highlights alignment between predicted and observed trends, red indicates a deviation, and orange denotes cases where the model predicted no meaningful change.

From the comparative analysis, it is evident that the KM model often struggles to accurately capture trends when the S:B ratio changes. This is particularly noticeable in cases where KM predictions remain static, failing to reflect experimental trends. This limitation is a significant contributor to KM's overall poor predictive performance, as also highlighted in other evaluation metrics such as RMSE values, scatter plots, and frequency distributions. For example, studies such as those by Yang et al. (2019), Loha et al. (2011), Nguyen et al. (2020), and Fremaux et al. (2015) demonstrate instances where KM predictions deviate or fail to capture variations in syngas composition driven by changes in S:B [58–61]. In contrast, NN exhibits a much higher degree of accuracy and consistency in capturing and predicting experimental trends across different studies and conditions.

Several studies included in Table 4 reveal instances where trend comparisons were not feasible due to the nature of the experimental setup. For example, Fremaux et al. (2015), Herguido et al. (1992), and Karatas et al. (2015) did not provide data for variations in temperature [61,69,70]. Similarly, S:B variation data wasn't included from Pinto et al. (2002), while Tuomi et al. (2015) and Jeremiáš et al. (2014) presented experimental conditions with simultaneous changes in multiple parameters, such as ER and CO_2:B, making trend-specific comparisons impractical [62,64,68]. Furthermore, Brachi et al. (2014) investigated conditions with simultaneous changes in both temperature and S:B, while Miccio et al. (2009) focused on the impact of different catalysts while maintaining constant temperature and S:B, limiting the feasibility of direct trend evaluation [73,74]. Despite these limitations in some studies, the NN model consistently outperforms KM in cases where comparisons are possible. NN aligns well with experimental trends, reflecting its ability to adapt to variations in both temperature and S:B. While KM struggles to adapt to changes in S:B and sometimes fails to predict significant variations, NN demonstrates significant agreement with experimental data.

3.4. Data generation

Total 3000 rows of synthetic data generation were conducted by the cGAN, as is described in section 2.3.3. The training progression of the cGAN demonstrated effective convergence and stable adversarial learning dynamics over two thousand epochs, as shown in Fig. S5. Initially, the discriminator loss was high (1.36 at epoch 0), reflecting its difficulty in distinguishing real data generated, while the generator loss started lower (0.67), indicating moderate success in producing realistic outputs. Over time, both losses stabilized within a narrow range, suggesting a balanced adversarial interplay between the two networks. Importantly, the MMD dropped significantly from 1.96 to as low as 0.07 (epoch 1800), confirming that the generated data progressively aligned with the statistical properties of the experimental dataset. The consistently low MMD values after approximately five hundred epochs indicate that the generator effectively learned the data distribution, yielding high-fidelity synthetic samples suitable for downstream SHAP and PDP interpretability analyses. Moreover, the comparison between the real/experimental data and synthetic data generated is shown in Fig. S6 and Fig. S7 which shows the similarity between the real and synthetic data.

Building on the successfully generated synthetic dataset, this study conducted a detailed sensitivity analysis to enhance the interpretability of the ML models and assess the influence of key gasification parameters on syngas composition. The synthetic data, closely aligned with the original experimental dataset, was employed as an extended input domain for the trained neural network models. This approach enabled a broader exploration of the feature space, effectively overcoming the limitations imposed by the relatively small size of the experimental dataset. By leveraging the enriched synthetic data, SHAP and PDP analyses were performed to uncover complex, non-linear relationships between inputs and outputs and to identify the most influential parameters governing the steam co-gasification process. This novel application of cGAN-generated data as a foundation for post hoc sensitivity analysis represents a key contribution of this work, providing valuable insights into the interpretability and robustness of the ML models.

3.5. Feature importance based on SHAP analysis

The SHAP analysis revealed several key findings, as illustrated in Fig. 6. For H_2, the S:B ratio was the most influential variable, highlighting the dominance of steam reforming reactions. The elemental composition of the feedstock, particularly oxygen, carbon, and hydrogen, also showed a positive influence, whereas ER exhibited a negative effect, consistent with its role in promoting complete combustion at the expense of H_2 yield. In the case of the CO the S:B has the adverse effect on the production indicating the steam reforming reactions is quite dominating again. For both H_2 and CO, increase in ER has negative influence as more ER ends up giving more CO_2. T (°C), ER, and S:B decreases CH_4 formation and is affected positively by the increasing carbon content. Reactor geometry, H cm and D cm, also contributed to variations in syngas composition, with H cm positively influencing H_2 and CO_2, while diameter showed an inverse effect. Given the varying concentration scales of different gas species, these mean

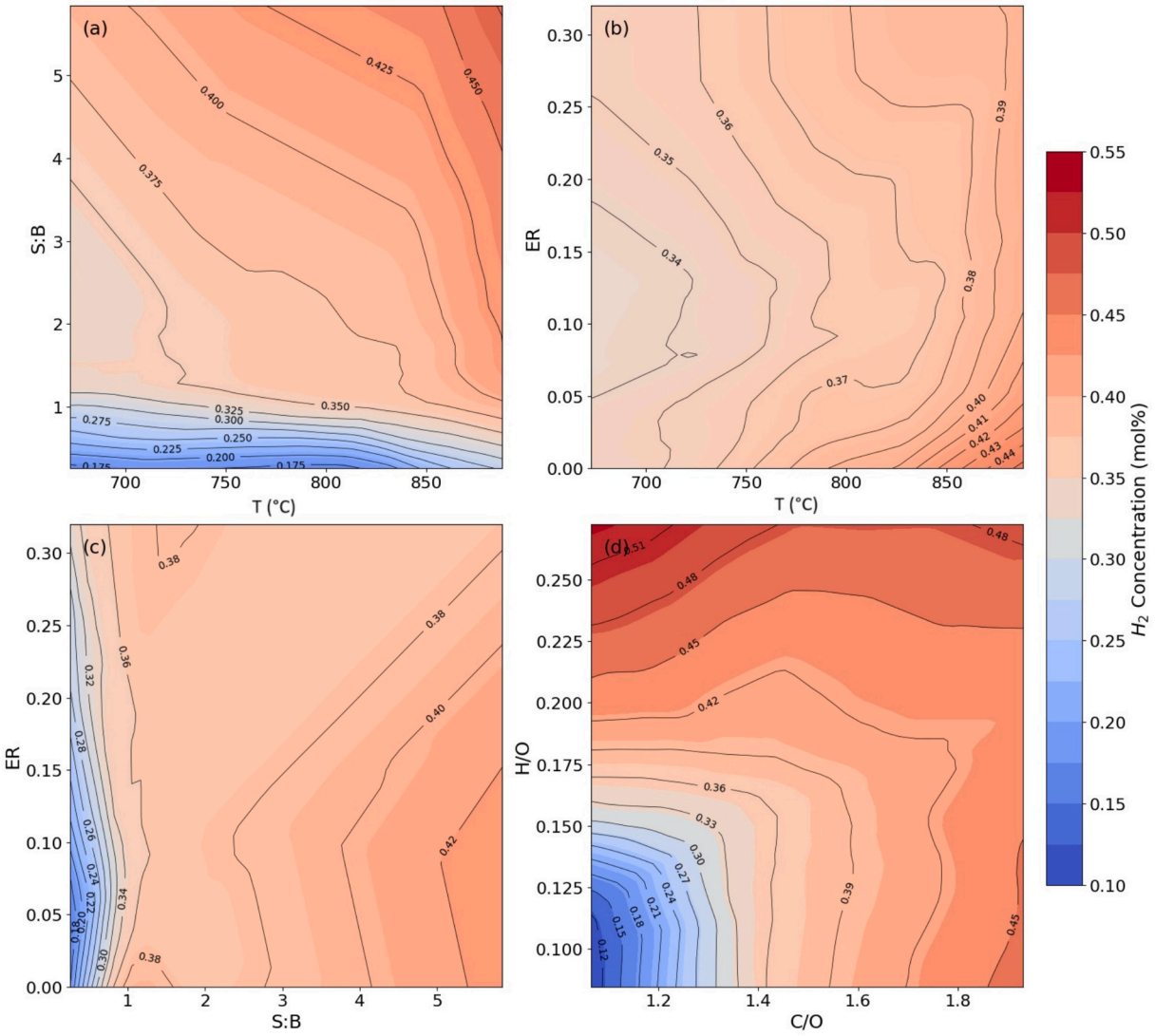

Fig. 8. Two-way PDP for H_2 concentration.

SHAP magnitudes were normalized in the radar plot of Fig. 7, enabling straightforward comparison of relative impacts, though it should be noted that this normalization can amplify the effect of outlying values.

3.6. Feature impact analysis by PDP

In practical experiments, isolating the effect of a single variable is difficult because altering one parameter often affects others. PDPs address this by illustrating the relationship between a chosen feature and syngas composition while holding all other inputs constant. To investigate how key process variables jointly influence syngas yields, 2D PDPs were generated for H_2 and CO. Fig. 8 presents the combined effect of operating conditions on H_2 concentration during steam co-gasification in a BFBG. In subplot (a), the combined influence of T and S:B is shown. H_2 concentration increases with both parameters, especially at elevated temperatures (>800 °C) and S:B ratios (>0.9). This aligns with the intensification of steam-promoted reactions such as the water-gas and methane reforming reactions. At low S:B and T (<0.9 and < 750 °C, respectively), H_2 concentration is lowest, emphasizing the limited reactivity under such conditions.

Subplot (b) examines the interaction between T (°C) and ER. H_2 concentration rises sharply at higher temperatures and lower ER values, indicating that excessive oxygen input (higher ER) suppresses H_2 through oxidation, while thermal activation promotes endothermic H_2-forming reactions. Subplot (°C) further confirms the negative influence of ER when combined with S:B. Even at high S:B values, low ER is necessary to maximize H_2, as oxygen-rich environments tend to consume H_2 via combustion. Lastly, subplot (d) illustrates the combined effect of carbon-to-oxygen (C/O) and hydrogen-to-oxygen (H/O) ratios in the feedstock. Higher H/O and moderate-to-high C/O ratios favor H_2 generation, highlighting the importance of feedstock chemistry. Notably, low H_2 yields are observed at low C/O and H/O ratios where insufficient reducing and hydrogenous content limits syngas hydrogen potential. This is a significant conclusion which shows that feedstock with higher H/O and C/O will give us higher H_2 concentration, as in the case of plastics.

Fig. 9 depicts the two-way PDPs, demonstrating how major process parameters influence CO concentration. In subplot (a), the interaction between T (°C) and S:B reveals that CO concentration is highest at moderate temperatures (~800 °C) and low S:B ratios (<1). This suggests that under low steam conditions, the water-gas shift and steam reforming reactions are less active, preserving CO. As S:B increases, CO is significantly consumed due to its conversion into H_2 and CO_2 via steam-promoted reactions. Subplot (b) shows the combined effect of T (°C) and ER, where CO concentrations decrease at higher ER levels, consistent with enhanced oxidation of CO to CO_2 in oxygen-rich environments. Peak CO values remain localized in low-ER and moderate-temperature regions.

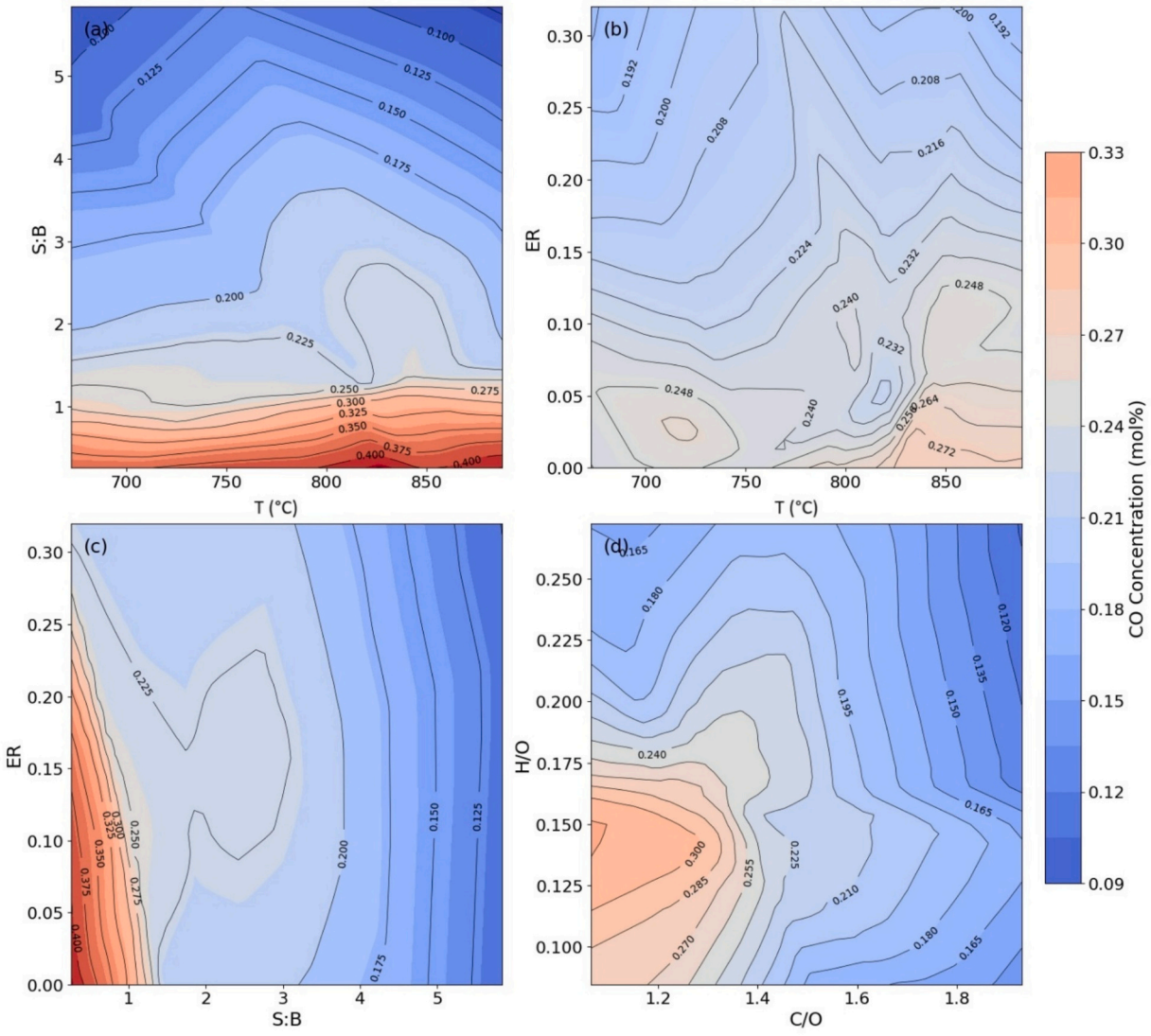

Fig. 9. Two-way PDP for CO concentration

In subplot T (°C), increasing S:B combined with higher ER leads to a pronounced drop in CO concentration, confirming that both oxygen and steam function as oxidizing/reactive agents reducing CO levels. At low ER and low-to-moderate S:B, CO retention is higher due to limited competing reactions.

3.7. Limitations and future work

Although the NN model consistently outperformed other ML and process simulator models, it is important to acknowledge its limitations. Being data-driven, its predictive reliability is constrained by the minimum and maximum ranges of the training data (Table S2). Predictions are most reliable within the overlap of the training and testing distributions, whereas extrapolation to extreme or unrepresented operating conditions, such as novel feedstocks not listed in Table S1 (e.g., biomass–coal or plastic–coal blends) or unusually high process input variables, remains uncertain. This limitation is inherent to most ML approaches and underscores the need for expanding the dataset. In future work, we aim to incorporate more diverse experimental data, including additional feedstocks and operating conditions, to strengthen the model's robustness and improve its generalizability across a wider range of process scenarios.

4. Conclusion

The co-gasification of biomass and solid waste represents a viable pathway toward sustainable energy production and carbon mitigation, yet accurate prediction of syngas composition remains challenging due to the inherent complexity of heterogeneous feedstocks and dynamic process conditions. This study provided a comprehensive comparison between first-principle models, including the TEM, RTM, and KM, and multiple ML approaches, such as RF, ET, kNN, XGB, SVM, and NN. The analysis was based on a diverse experimental dataset compiled from twenty published studies encompassing a wide range of feedstock and gasifying agents (steam and O_2). Following robust data preprocessing and model training, results showed that ML models, particularly NN, significantly outperformed traditional simulation models across all target outputs, with NN achieving the lowest average RMSE (0.0174) compared to RTM (0.09668), TEM (0.147), and KM (0.137). Notably, while RTM showed robust performance for predictions of H_2 and CO, NN consistently delivered higher accuracy across all outputs, underscoring its ability to capture non-linear and multivariate interactions within the data.

Beyond predictive accuracy, the integration of explainable ML tools (SHAP values and PDP) provided transparent mechanistic insights, confirming, for instance, that higher S:B ratios strongly favor H_2

generation, while elevated equivalence ratios ER drive CO_2 formation. The PDP analysis further clarified how H_2 yields are affected by process variables and provided insights into the expected H_2 concentrations based on specific H/O and C/O ratios in the feedstock. These interpretability results are particularly valuable for guiding process optimization and operational decision-making.

From a scalability perspective, Aspen Plus-based models remain crucial for process design and scale-up studies. On the other hand, NN possess real time control potential through their ability to learn nonlinear dynamics and provides rapid, adaptive responses of complex co-gasification process. The accuracy demonstrated translates to more reliable process control strategies, which could, in practice, enhance syngas yields and improve overall carbon utilization efficiency. By reducing reliance on exhaustive experimental campaigns and accelerating process optimization, the proposed framework supports effective development of biomass–plastic valorization systems.

CRediT authorship contribution statement

Usman Khan Jadoon: Writing – original draft, Visualization, Validation, Software, Methodology, Funding acquisition, Formal analysis, Data curation. **Ismael Díaz:** Writing – review & editing, Validation, Supervision, Software, Resources, Project administration, Formal analysis, Conceptualization. **Manuel Rodríguez:** Writing – review & editing, Validation, Supervision, Resources, Project administration, Formal analysis, Conceptualization.

Declaration of competing interest

The authors declare that they have no known competing financial interests or personal relationships that could have appeared to influence the work reported in this paper.

Acknowledgements

This work was co-funded by Repsol and the European Union's Horizon 2020 Marie Skłodowska-Curie program (Grant Agreement No. 945139), under the "SDGine for Healthy People and Cities" initiative. Ismael Díaz and Manuel Rodríguez thank support from Comunidad de Madrid under the AgroSUSTEC-CM project (TEC-2024/BIO-27).

Appendix A. Supplementary data

Supplementary data to this article can be found online at https://doi.org/10.1016/j.fuproc.2025.108340.

Data availability

The data that has been used in the data is given in Supplementgary data, attached to the main article.

References

[1] D. Gielen, et al., Global Energy Transformation: A Roadmap to 2050, 2019.
[2] IEA, U, Global Energy Review 2020. Ukraine, Online, https://www.iea.org/countries/ukraine. Accessed: 2020-09-10, 2020, p. 810.
[3] P.N.Y. Yek, et al., Co-processing plastics waste and biomass by pyrolysis–gasification: a review, Environ. Chem. Lett. 22 (1) (2024) 171–188.
[4] G. Schuster, et al., Biomass steam gasification–an extensive parametric modeling study, Bioresour. Technol. 77 (1) (2001) 71–79.
[5] S. Iannello, S. Morrin, M. Materazzi, Fluidised bed reactors for the thermochemical conversion of biomass and waste, Kona Powder Part. J. 37 (2020) 114–131.
[6] U. Arena, et al., A techno-economic comparison of fluidized bed gasification of two mixed plastic wastes, Waste Manag. 31 (7) (2011) 1494–1504.
[7] U. Arena, Process and technological aspects of municipal solid waste gasification. A review, Waste Manag. 32 (4) (2012) 625–639.
[8] A. Gómez-Barea, B. Leckner, Modeling of biomass gasification in fluidized bed, Prog. Energy Combust. Sci. 36 (4) (2010) 444–509.
[9] K. Kwong, E. Marek, Combustion of biomass in fluidized beds: a review of key phenomena and future perspectives, Energy Fuel 35 (20) (2021) 16303–16334.
[10] J. Delgado, M.P. Aznar, J. Corella, Biomass gasification with steam in fluidized bed: effectiveness of CaO, MgO, and CaO− MgO for hot raw gas cleaning, Ind. Eng. Chem. Res. 36 (5) (1997) 1535–1543.
[11] C. Courson, et al., Development of Ni catalysts for gas production from biomass gasification. Reactivity in steam- and dry-reforming, Catal. Today 63 (2–4) (2000) 427–437.
[12] P. Mathieu, R. Dubuisson, Performance analysis of a biomass gasifier, Energy Convers. Manag. 43 (9–12) (2002) 1291–1299.
[13] C. Wu, et al., Analysis of biomass gasification for MHV fuel gas, Gas Heat 2 (1995) 8–14.
[14] S. Kajitani, S. Hara, H. Matsuda, Gasification rate analysis of coal char with a pressurized drop tube furnace, Fuel 81 (5) (2002) 539–546.
[15] N. Sadhwani, S. Adhikari, M.R. Eden, Biomass gasification using carbon dioxide: effect of temperature, CO_2/C ratio, and the study of reactions influencing the process, Ind. Eng. Chem. Res. 55 (10) (2016) 2883–2891.
[16] Y. Shen, et al., CO_2 gasification of woody biomass: Experimental study from a lab-scale reactor to a small-scale autothermal gasifier, Energy 170 (2019) 497–506.
[17] G. Flori, et al., Experimental assessment of oxy-CO_2 gasification strategy with woody biomass, Renew. Energy 228 (2024) 120593.
[18] K. Paavani, et al., Advances in plastic to fuel conversion: reactor design, operational optimization, and ML integration, Sustain. Energy Fuels 9 (1) (2025) 54–71.
[19] M. Ajorloo, et al., Modeling and experimental validation of the Co-gasification of plastic and biomass waste to estimate product yields, Energy 317 (2025) 134718.
[20] H. Shi, et al., Modeling of biomass gasification for fluidized bed in Aspen Plus: using ML for fast pyrolysis prediction, Energy Convers. Manag. 332 (2025) 119695.
[21] U.K. Jadoon, I. Díaz, M. Rodríguez, Comparative analysis of aspen plus simulation strategies for woody biomass air gasification processes, Biomass Bioenergy 194 (2025) 107626.
[22] A. Bhattarai, H. Khodaei, S. Adhikari, Oxy-steam fluidized bed co-gasification of plastic wastes and biomass: experimental study and CFD simulation, Waste Manag. 204 (2025) 114931.
[23] S. Gupta, et al., Large eddy simulation of biomass gasification in a bubbling fluidized bed based on the multiphase particle-in-cell method, Renew. Energy 163 (2021) 1455–1466.
[24] A. Wodołażski, A. Smoliński, Modeling and process integration study of dimethyl ether synthesis from syngas derived from biomass gasification: Flowsheet simulation, Alex. Eng. J. 59 (6) (2020) 4441–4448.
[25] J.J. Escalante, et al., Prediction construction for biomass and high-density polyethylene co-gasification via statistical method and ML, Fuel 391 (2025) 134828.
[26] A.M.A. Ahmed, et al., Review of kinetic and equilibrium concepts for biomass tar modeling by using Aspen Plus, Renew. Sust. Energ. Rev. 52 (2015) 1623–1644.
[27] M. Niu, et al., Simulation of syngas production from municipal solid waste gasification in a bubbling fluidized bed using Aspen Plus, Ind. Eng. Chem. Res. 52 (42) (2013) 14768–14775.
[28] L. Zhu, et al., MSW to synthetic natural gas: system modeling and thermodynamics assessment, Waste Manag. 48 (2016) 257–264.
[29] M. Shahbaz, et al., Syngas production from steam gasification of palm kernel shell with subsequent co2 capture using CaO sorbent: an aspen plus modeling, Energy Fuel 31 (11) (2017) 12350–12357.
[30] A. Abdelrahim, et al., Experimental and numerical investigation of biosolid gasification: Equilibrium-based modeling with emphasis on the effects of different pretreatment methods, Ind. Eng. Chem. Res. 59 (1) (2019) 299–307.
[31] M. Ajorloo, et al., Recent advances in thermodynamic analysis of biomass gasification: a review on numerical modeling and simulation, J. Energy Inst. 102 (2022) 395–419.
[32] M. Singh, et al., Simulation of biomass-plastic co-gasification in a fluidized bed reactor using Aspen plus, Fuel 319 (2022) 123708.
[33] F.-H. Wu, Y.-T. Hsu, Parameter study of waste shiitake substrate/waste polyethylene Co-gasification using Aspen Plus kinetic modeling, Int. J. Hydrog. Energy 83 (2024) 29–38.
[34] Y. Cao, Y. Bai, J. Du, H2-rich gas production from co-gasification of biomass/plastics blends: a modeling approach, J. Energy Inst. 112 (2024) 101454.
[35] S.M. Beheshti, H. Ghassemi, R. Shahsavan-Markadeh, Process simulation of biomass gasification in a bubbling fluidized bed reactor, Energy Convers. Manag. 94 (2015) 345–352.
[36] M.B. Nikoo, N. Mahinpey, Simulation of biomass gasification in fluidized bed reactor using ASPEN PLUS, Biomass Bioenergy 32 (12) (2008) 1245–1254.
[37] N.M. Nguyen, F. Alobaid, B. Epple, Process simulation of steam gasification of torrefied woodchips in a bubbling fluidized bed reactor using aspen plus, Appl. Sci. 11 (6) (2021) 2877.
[38] M. Cakar, et al., Utilization of ML algorithms in estimation of syngas fractions and exergy values for gasification of biomass-lignite mixtures in fixed and fluidized bed gasifiers, Fuel 401 (2025) 135883.
[39] J. Salisu, et al., Modeling of sustainable methanol production via integrated co-gasification of rice husk and plastic coupled with its prediction and optimization using ML and statistical-based models, J. Energy Inst. 120 (2025) 102029.
[40] Y. Yang, et al., Predicting municipal solid waste gasification using ML: a step toward sustainable regional planning, Energy 278 (2023) 127881.
[41] P.J.G. Lisboa, et al., The coming of age of interpretable and explainable ML models, Neurocomputing 535 (2023) 25–39.
[42] P. Xue, et al., Prediction of syngas properties of biomass steam gasification in fluidized bed based on ML method, Int. J. Hydrog. Energy 49 (2024) 356–370.

[43] K. Khandelwal, S. Nanda, A.K. Dalai, ML modeling of supercritical water gasification for predictive hydrogen production from waste biomass, Biomass Bioenergy 197 (2025) 107816.
[44] D.S. Pandey, H. Raza, S. Bhattacharyya, Development of explainable AI-based predictive models for bubbling fluidised bed gasification process, Fuel 351 (2023) 128971.
[45] T. Vaiyapuri, Optimizing hydrogen production in the co-gasification process: comparison of explainable regression models using shapley additive explanations, Entropy 27 (1) (2025) 83.
[46] L.P.R. Pala, et al., Steam gasification of biomass with subsequent syngas adjustment using shift reaction for syngas production: an Aspen Plus model, Renew. Energy 101 (2017) 484–492.
[47] M.C. Acar, Y.E. Böke, Simulation of biomass gasification in a BFBG using chemical equilibrium model and restricted chemical equilibrium method, Biomass Bioenergy 125 (2019) 131–138.
[48] D.J. Roddy, C. Manson-Whitton, 5.10 - biomass gasification and pyrolysis, in: A. Sayigh (Ed.), Comprehensive Renewable Energy, Elsevier, Oxford, 2012, pp. 133–153.
[49] D. Neves, et al., Characterization and prediction of biomass pyrolysis products, Prog. Energy Combust. Sci. 37 (5) (2011) 611–630.
[50] M. Harussani, et al., Pyrolysis of polypropylene plastic waste into carbonaceous char: Priority of plastic waste management amidst COVID-19 pandemic, Sci. Total Environ. 803 (2022) 149911.
[51] I. Goodfellow, et al., Generative adversarial networks, Commun. ACM 63 (11) (2020) 139–144.
[52] M. Mirza, S. Osindero, Conditional generative adversarial nets, ArXiv (2014), https://doi.org/10.48550/arXiv.1411.1784, 1411.1784.
[53] A. Ganguly, R.C. Brown, M.M. Wright, Investigating the impacts of feedstock variability on a carbon-negative autothermal pyrolysis system using ML, Front. Climate 4 (2022) 842650.
[54] S.M. Lundberg, S.-I. Lee, A unified approach to interpreting model predictions, Adv. Neural Inf. Proces. Syst. 30 (2017).
[55] L.S. Shapley, A Value for n-person Games, 1953.
[56] J.H. Friedman, Function trees: Transparent machine learning, ArXiv 2 (2024), https://doi.org/10.48550/arXiv.2403.13141, 2403.13141.
[57] M. Pilar González-Vázquez, et al., Thermodynamic analysis of biomass gasification using aspen plus: Comparison of stoichiometric and non-stoichiometric models, Energies 14 (1) (2021) 189.
[58] H. Yang, et al., Experimental research for biomass steam gasification in a fluidized bed, Energy Sources, Part A 41 (16) (2019) 1993–2006.
[59] C. Loha, P.K. Chatterjee, H. Chattopadhyay, Performance of fluidized bed steam gasification of biomass – Modeling and experiment, Energy Convers. Manag. 52 (3) (2011) 1583–1588.
[60] N.M. Nguyen, et al., Experimental study on steam gasification of torrefied woodchips in a bubbling fluidized bed reactor, Energy 202 (2020) 117744.
[61] S. Fremaux, et al., An experimental study on hydrogen-rich gas production via steam gasification of biomass in a research-scale fluidized bed, Energy Convers. Manag. 91 (2015) 427–432.
[62] S. Tuomi, et al., Behaviour of tars on the filter in high temperature filtration of biomass-based gasification gas, Fuel 139 (2015) 220–231.
[63] F. Pinto, et al., Effect of gasification agent on co-gasification of rice production wastes mixtures, Fuel 180 (2016) 407–416.
[64] M. Jeremiáš, et al., Ammonia yield from gasification of biomass and coal in fluidized bed reactor, Fuel 117 (2014) 917–925.
[65] M. Jeremiáš, et al., Gasification of biomass with CO_2 and H_2O mixtures in a catalytic fluidised bed, Fuel 210 (2017) 605–610.
[66] S. Pecate, et al., Beech wood gasification in a dense and fast internally circulating fluidized bed, Fuel 236 (2019) 554–573.
[67] M.K. Karmakar, A.B. Datta, Generation of hydrogen rich gas through fluidized bed gasification of biomass, Bioresour. Technol. 102 (2) (2011) 1907–1913.
[68] F. Pinto, et al., Co-gasification study of biomass mixed with plastic wastes, Fuel 81 (3) (2002) 291–297.
[69] J. Herguido, J. Corella, J. Gonzalez-Saiz, Steam gasification of lignocellulosic residues in a fluidized bed at a small pilot scale. Effect of the type of feedstock, Ind. Eng. Chem. Res. 31 (5) (1992) 1274–1282.
[70] H. Karatas, F. Akgun, Experimental results of gasification of walnut shell and pistachio shell in a bubbling fluidized bed gasifier under air and steam atmospheres, Fuel 214 (2018) 285–292.
[71] M.S. Masnadi, et al., Single-fuel steam gasification of switchgrass and coal in a bubbling fluidized bed: a comprehensive parametric reference for co-gasification study, Energy 80 (2015) 133–147.
[72] J. Udomsirichakorn, et al., Effect of CaO on tar reforming to hydrogen-enriched gas with in-process CO_2 capture in a bubbling fluidized bed biomass steam gasifier, Int. J. Hydrog. Energy 38 (34) (2013) 14495–14504.
[73] P. Brachi, et al., Fluidized bed co-gasification of biomass and polymeric wastes for a flexible end-use of the syngas: Focus on bio-methanol, Fuel 128 (2014) 88–98.
[74] F. Miccio, et al., Biomass gasification in a catalytic fluidized reactor with beds of different materials, Chem. Eng. J. 154 (1) (2009) 369–374.
[75] F. Pinto, et al., Effects of experimental conditions and of addition of natural minerals on syngas production from lignin by oxy-gasification: Comparison of bench- and pilot scale gasification, Fuel 140 (2015) 62–72.
[76] H. Jiang, et al., CPFD modeling of air-steam gasification of brewer's spent grains in a bubbling fluidized bed, Fuel 372 (2024) 132132.